




Article

# Investigation of a Small Landslide in the Qinghai-Tibet Plateau by InSAR and Absolute Deformation Model

Junming Hao <sup>1,2,4</sup> , Tonghua Wu <sup>1,\*</sup> , Xiaodong Wu <sup>1</sup>, Guojie Hu <sup>1</sup>, Defu Zou <sup>1</sup>, Xiaofan Zhu <sup>1</sup>, Lin Zhao <sup>3</sup>, Ren Li <sup>1</sup>, Changwei Xie <sup>1</sup> , Jie Ni <sup>1</sup>, Cheng Yang <sup>1</sup>, Xiangfei Li <sup>1</sup> and Wensi Ma <sup>1</sup>

<sup>1</sup> Cryosphere Research Station on the Qinghai-Tibet Plateau, State Key Laboratory of Cryospheric Sciences, Northwest Institute of Eco-Environment and Resources, Chinese Academy of Sciences, Lanzhou 730000, China; haojm198@lzb.ac.cn (J.H.); wuxd@lzb.ac.cn (X.W.); huguojie123@lzb.ac.cn (G.H.); defuzou@lzb.ac.cn (D.Z.); zxf\_jc@lzb.ac.cn (X.Z.); liren@lzb.ac.cn (R.L.); xiecw@lzb.ac.cn (C.X.); jieni@lzb.ac.cn (J.N.); 12yangcheng@lzb.ac.cn (C.Y.); lixiangfei18@mails.ucas.ac.cn (X.L.); wanglisha@lzb.ac.cn (W.M.)

<sup>2</sup> School of Civil Engineering, Lanzhou University of Technology, Lanzhou 730050, China

<sup>3</sup> School of Geographical Sciences, Nanjing University of Information Science & Technology, Nanjing 210044, China; linzhao@lzb.ac.cn

<sup>4</sup> University of Chinese Academy of Sciences, Beijing 100049, China

\* Correspondence: thuawu@lzb.ac.cn

Received: 31 July 2019; Accepted: 5 September 2019; Published: 12 September 2019



**Abstract:** Landslides are one of the major geohazards in the Qinghai-Tibet Plateau, and have recently increased in both frequency and size. SAR interferometry (InSAR) has been widely applied in landslide research, but studies on monitoring small-scale landslides are rare. In this study, we investigated the performance of Small Baseline Subsets method (SBAS) in monitoring small-scale landslide and further developed a new deformation model to obtain the absolute deformation time series. The results showed that SBAS could well capture the small-scale landslide characteristics including spatiotemporal abnormal displacement and progressive failure processes. The newly developed absolute deformation model further detected the process of landslide details, such as instances of noticeable creeps induced by rainfall and snowmelt. Finally, a conceptual model of the kinematics-based failure mechanism for small-scale landslide was proposed. This study extended the monitoring capability of InSAR and improved our knowledge on the deformation in the frozen ground regions.

**Keywords:** landslide; SAR interferometry (InSAR); Small Baseline Subsets (SBAS); absolute deformation; Qinghai-Tibet Plateau

## 1. Introduction

Due to the area's intense tectonic activity, complex geomorphology, and climate change, the Qinghai-Tibet Plateau (QTP) is vulnerable to geohazards [1]. One of the most common geohazards is landslide. Recent studies have found that a warmer climate and more frequent extreme climate events in the QTP may cause landslides to occur more frequently [2,3]. In frozen ground regions, it got much worse. The climate change weakened the inherent stability of frozen ground [4]. The freeze thaw cycle made shallow deposits creep continuously and the loss of ice changes the fundamental behavior of the slope [5,6]. The events of landslide have significantly accelerated the alpine ecosystem degradation [7], desertification [8], and destabilization of human infrastructure [9,10]. Fatal landslide events are recorded in the Emergency Events Database [11] and the China Statistical Yearbook [12],

but smaller landslides ( $<10^5 \text{ m}^3$ ) [13] are rarely documented because of the lack of data available for monitoring, research and prediction [14]. While the events of small-scale slope instability can be seen everywhere in Qinghai-Tibet Plateau, even at a slope of  $4\text{--}9^\circ$  [15]. Even a minimal change, such as a small-scale landslides in the land surface can influence the surface environment through various processes such as radiation and water and heat exchange [16]. Therefore, it is vital to monitor the short- and long-term effects of landslides [17].

Multiple techniques have been employed in small-scale landslides investigations and analysis [18,19], such as (1) generating landslide inventories using Airborne Lidar Data [20], (2) evaluating susceptibility mapping with digital elevation models (DEMs) [21], (3) analyzing the temporal evolution with aerial photogrammetry [22], and (4) surveying the critical threshold for reactivating the landslide with geophysics [23]. In recent years, the high-resolution Synthetic Aperture Radar interferometry technique (InSAR) has proven to be an excellent tool to monitor the landslide on both the site-specific and the regional scale, including landslide hazard investigation, landslide monitor and landslide prediction [24–27]. Although the rapid movement of landslide and terrain effect lead to the decorrelation of SAR data, InSAR still represents one possibility for mapping surface deformation at fine spatial resolution over large areas in order to characterize aspects of terrain motion and potentially hazardous processes [28], in alpine mountainous regions such as the Apennines [24], Alps [29] and the Andes [28]. However, the InSAR using in the Qinghai-Tibet Plateau aiming for small-scale landslide events are rare.

Challenges persist regarding the practical applicability of InSAR to landslide investigations [30,31]. Coherence loss and atmospheric effects are the most important factors that limit the utility of many currently available radar satellite datasets [32]. Therefore, a lot of advanced techniques have been proposed for landslide analysis, including Permanent Scatters (PS) [33] and Small Baseline Subsets (SBAS) [34]. PS can detect the dominant radar targets, but loses the ability to monitor wide areas. SBAS allows for the construction of large-scale deformation maps and the analysis of landslide formation and development [34,35]. An additional limit of InSAR is that the deformation amount inferred from the number of fringes are relative changes, not absolute changes relative to zero deformation [36].

In our study, we employed the SBAS method and the absolute deformation model to monitor surface displacement in landslide area using Sentinel-1 data (2016–2017) [37], and further developed a kinematic model to explain the formation of small-scale landslide, and then discussed the results. The objective of our study is investigating to the performance of InSAR (SBAS) method in monitoring small-scale landslide, and discussing the quality of absolute deformation model in signal separation process.

## 2. Study Area

The study area is a 12 km by 12 km (Figure 1b) section of the eastern QTP, south of the Bayan Har Mountains. With an average elevation of 4570 m above sea level, this area is characterized by snow-covered peaks, developed snow and river erosion, and a Triassic sand-slate lithology. In this area, earthquake-prone is related to the Ganzi-Yushu NW-SE faults [38]. The valley is “V” shaped gradually shrinking towards the north-east. The watershed of Yangtze River and Yellow River is located. Recent field investigations (Figure 1c,d) indicate that near-surface deposits are dominated by weathered bedrock and residual slope sediments, prone to collapse and landslide. The soil contains a large amount of organic matter and sand. Data records from the nearest meteorological station (Figure 1a) show that this plateau continental climate experienced a mean annual air temperature of  $-4.8^\circ\text{C}$  and an annual precipitation of 503 mm from June to September from 1971 to 2007. The snow cover in Yushu with 5–10 cm depth is from November to April and still exists in ridges or valleys after June [39]. Both show increasing trends. The alpine meadow is the main vegetation type, and its coverage is close to 40%. The seasonally frozen areas have a strong freeze thaw cycle, and the permafrost are widely distributed (over  $\sim 4600 \text{ m}$ ) as islands in the mountains and strips in the valley area [40]. The depth of seasonal freezing is about 2.5 m [41].

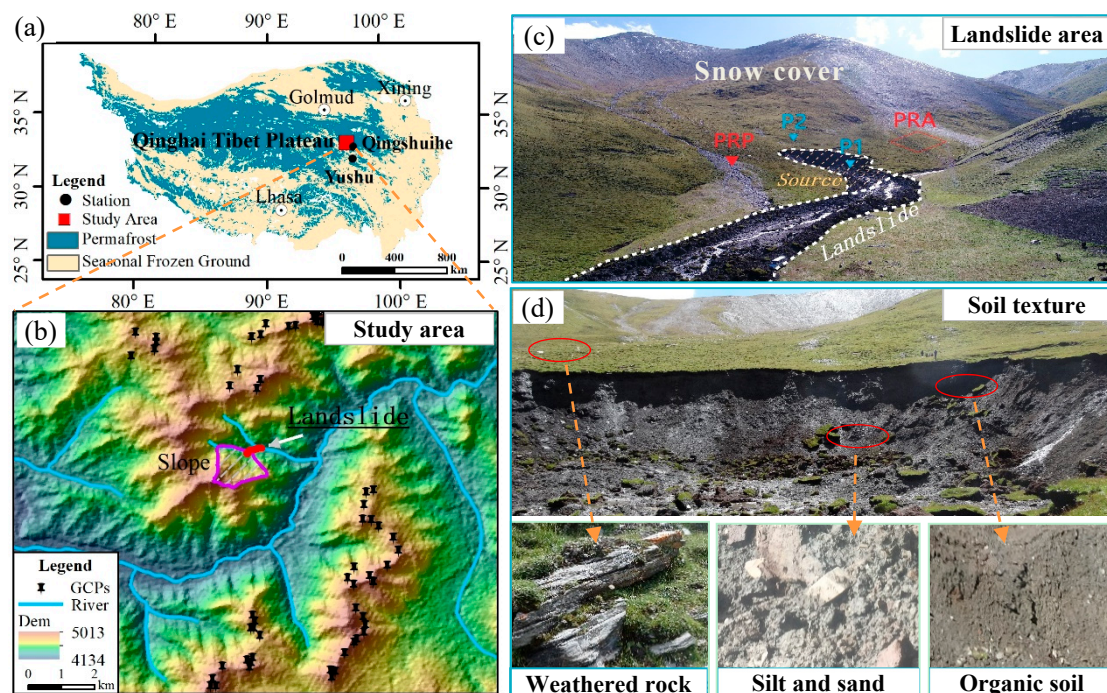


**Figure 1.** Location, topography(b) and soil texture (d) of the landslide site (c) in study area in the Qinghai-Tibet Plateau (a). The permafrost distribution modified from [40] GCPs are the ground control points prepared for InSAR processing. Coherent points (P1 and P2) detected by InSAR. Zero-reference point (PrP) and zero-reference area (PrA) around the landslide.

On 7 September 2017, a small landslide ( $34^{\circ}07'06''$  N,  $96^{\circ}37'15''$  E, 4433 m above sea level) broke out on lower and gentle slopes ( $5\text{--}10^{\circ}$ ) in Chenduo County (Figure 1). Investigating by the unmanned aerial vehicle and metal ruler, the landslide with a volume of about  $2.4 \times 10^4$  m<sup>3</sup> covered about  $1.6 \times 10^4$  m<sup>2</sup> where a deep pit formed a diameter of about 70 m, the head wall of landslide was more than 8.5 m thick, the sliding length was about 397 m, the average width was about 32 m and the deposit. Due to the continuous rainfall, the ground suddenly split, pushed a column of humus about 3 m thick along the riverbed, and formed the landslide and debris flow. We did not discover the under-ground ice in the landslide area. The sliding process was uploaded to the internet and received much attention from government and people [42,43].

Strictly speaking, the landslide typology is an earthflow per The Landslide Handbook [44] and usually associated with triggered by rainfall events. From the Google Earth images in Figure S1, there were two collapses in the central part of the landslide area before 2010 and expanded into a fracture network in 2016. The length of the crack increased from 43 m in 2010 to 50 m in 2016.

### 3. Datasets and Processing

#### 3.1. Digital Elevation Models (DEM) Producing

ASTER GDEM (ASTGTM2-N33E96, ASTGTM2-N33E97, ASTGTM2-N34E96 and ASTGTM2-N34E97) with a resolution of 30 m, was released by the United States Geological Survey (USGS) [45]. As a digital expression of earth surface, DEM was used to estimate and remove the topographic phase in InSAR processing.

On 10 September 2017, after the landslide had occurred, a quad-rotor unmanned aerial vehicle (UAV; PHANTOM 4 PRO) [46] was used to acquire DEM data. The UAV images had an average ground resolution of 30 cm, an overlap rate of 70–80% on the heading and lateral sides, and an altitude of 100 m from the ground level. We created DEM images using Smart3D, a close-range photogrammetry

software. The error threshold was 0–0.4 m in horizontal direction and 0–0.5 m in height direction based on photo-control-point. The UAV data was used to investigate the landslide site.

### 3.2. Short Baseline Interferometry

A total of 27 scenes of ascending Sentinel-1A SLC frames were acquired from 16 January 2016 to 19 September 2017. The frames were acquired with the same look angle and path. The detailed parameters for our SAR data are listed in Table 1.

**Table 1.** The acquisition parameters of Synthetic Aperture Radar (SAR) data.

SAR Sensor	Sentinel-1A IW SLC
Orbit direction	Ascending
Microwave band (polarization)	C-band (VV)
Number of frames	27
Resolution	5 m × 20 m
Repeat cycle	12 days
Look angle	42°
Temporal coverage	January 2016–September 2017

Note: Data were downloaded from European Space Agency [37].

By measuring the phase difference between two SAR frames taken at different times, we used InSAR to construct a series of interferograms, which showed the ground surface displacement in the line-of-sight (LOS) direction.

Because of the complex topography, we used critical time baselines of 100 days, respectively, to generate each graph. In the final graph (Figure 2), the spatial baselines were 6–145 m and the time baselines were 12–84 days. These baselines make the topographic phase suppression easier, and reduce the effects of spatial decorrelation [26]. In the end, we produced 89 interference pairs.

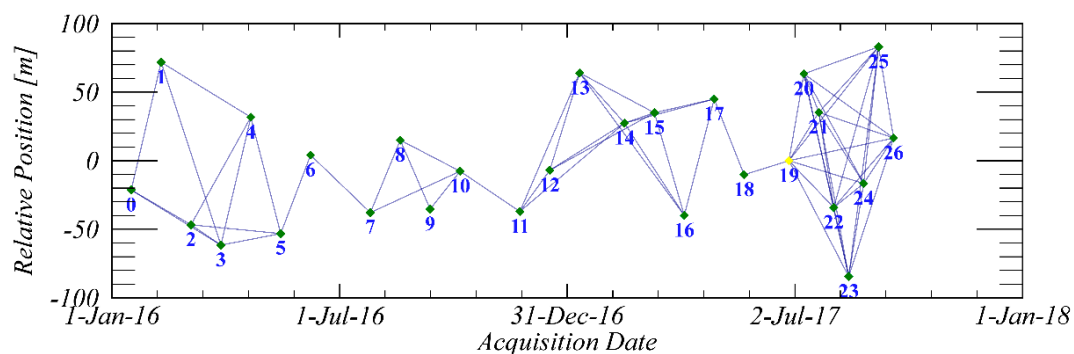


**Figure 2.** Spatial temporal baselines for the interferograms. Points represent SAR frames listed in Table S1 and numbered lines are the interferometric pairs.

We then built interferograms as a way to illustrate the cumulative deformation of the region [34]. In computing a generic  $i$ -interferogram, with a pixel of azimuth and range coordinates  $(x, r)$ , from the SAR acquisitions at times  $t_1$  and  $t_2$ , the topographic phase component removal is given by the following equations:

$$\begin{aligned} \delta\varphi_i &= \varphi(t_2, x, r) - \varphi(t_1, x, r) \\ &\approx \frac{4\pi}{\lambda} [d(t_2, x, r) - d(t_1, x, r)] + \Delta\varphi_i^{atm}(t_1, t_2, x, r) + \Delta\varphi_i^{topo}(x, r) \end{aligned} \quad (1)$$

where  $\lambda$  is the signal central wavelength of Sentinel-1A,  $d(t_1, x, r)$  and  $d(t_2, x, r)$  are the line-of-sight (LOS) cumulative deformation at times  $t_1$  and  $t_2$ ,  $\Delta\varphi_i^{atm}$  is the atmospheric phase caused by atmospheric

disturbance, and  $\Delta\varphi_i^{topo}$  is the topographic phase. Assuming that  $d(t_0, x, r) = 0$  and that the SBAS deformation is relative:

$$\Delta\varphi_i^{topo}(x, r) = -\frac{4\pi B_{\perp i}\Delta z(x, r)}{\lambda r \sin\theta} \quad (2)$$

This term accounts for possible phase artifacts caused by an error in the knowledge of the scene topography; note that the impact of these artifacts depends on the orbit separation component  $B_{\perp i}$  (usually referred to as perpendicular baseline),  $\Delta z(x, r)$ , the target of elevation on the land surface (DEM), and on the incidence angle  $\theta$  of the SAR.

Before the critical step of phase unwrapping, we applied three important corrections to improve the data signal-to-noise ratio. (1) We remove the phase delay based on an Atmospheric Phase Screen (APS) using the global atmospheric reanalysis model [47]. At an elevation of 4500 m in a dry environment, turbulent APS is moderate at lower elevations [48]. (2) We selected 69 ground control points (GCPs) with coherence greater than 0.8 on the bedrock of the mountaintop and precise satellite orbits [49] to remove the residual orbital errors and the effects of clock drift [50]. (3) We also corrected the effect of digital elevation model (DEM) errors [51]. However, the normal baseline value is less than 150 m, strongly limiting the impact of DEM errors [52]. When the baselines can be quite large, e.g., ALOS PALSAR, an accurate DEM must be used to remove the topographic phase [53].

In order to unwrap the phase, we implement a minimum workflow algorithm [54] to reduce the noise on the wrapped phase for further processing. The application of the singular value decomposition method allows us to separate the large baselines to improve the temporal sampling rate [34]. Then, we removed 25 interferometric pairs with low coherence, poor phase unwrapping, and large atmospheric disturbances from the dataset and used 64 high-quality pairs (Figure 2) for further inversion. Considering the complex terrain conditions and the climate characteristics related to the landslide, the coherence threshold for each pixel was set to 0.2 [26].

Finally, the unwrapped phase ( $\varphi_{disp}$ ) was then translated into the LOS displacement ( $d$ ) and the vertical displacement ( $d_v$ ) using the following equations [53,55]:

$$\varphi_{disp} = \frac{4\pi}{\lambda} d \quad (3)$$

$$d_v = \frac{\varphi_{disp}}{\cos\theta} \quad (4)$$

and subsequently the displacement geocoded into a map projection as pixels and points. A pixel or point represented a spatial area of about 20 m  $\times$  20 m. We clipped a 12 km  $\times$  12 km subset of that area (Figure 1b) for our landslide research.

### 3.3. Calculation of Absolute Surface Displacements

InSAR is limited to only measuring the relative surface deformation due to the  $2\pi$  ambiguity problem, the satellite orbit errors, and the GCPs. We also wanted to quantify the absolute displacement differences (ADD) between the landslide and the surrounding areas. While in case of calculation of absolute surface displacement an observer needed to take into interferogram zero-reference surface or known velocity [38]. We assumed that adjacent areas with similar local conditions (LCs) (i.e., similar altitude, geology, soil, climate, and freeze thaw cycles) would experience similar surface deformation processes during the study period. In order to analyze the difference, we separated the SAR signal by considering the freeze thaw cycles and local conditions. Then, we selected a reference point (PrP) and reference area (PrA) as a zero-reference (Figure 1c), both of which were adjacent to the landslide, to define the surface movement of landslide. The P1 and P2 as representative points were the indicators of landslide movements.

The PrP with the small annual rates represented the freeze thaw cycles. In frozen ground regions, the seasonal ground displacement of active layer caused by the freezing and thawing process [56]. The displacement contained a secular part and a seasonal part, assuming that the seasonal displacement

was proportional to the accumulated degree days of thaw or freezing [45,51]. A sinusoidal function with a first-order and linear was used here to map variations of the amplitude of the seasonal signal and the time of the thaw-subsidence and freezing-rise [48,57,58]. The function was as follows:

$$D_1(t) = C_1 + Kt + A \sin\left(\frac{2\pi}{T}t - \varphi\right) \quad (5)$$

where  $D$  is the displacement (mm) monitoring by InSAR,  $A$  is the amplitude (mm),  $T$  is the period of freezing or melting,  $\varphi$  is the initial phase (rad) and  $t$  was the number of days since January 2016.  $Kt$  was the secular displacement and  $C_1$  is constant. Considering the PrP with the short period (less than 2 years) and small annual rates (less than 5 mm/yr), we set  $C_1$  and  $K$  equal to 0. Then the solution of the equation can be written as follows:

$$D_1(t) = A \sin\left(\frac{2\pi}{T}t - \varphi\right) \quad (6)$$

The PrA area represented the surface deformation process affected by LCs. This area was about 100 m from the landslide, had the same elevation as the landslide, and a lateral extent of 100 m  $\times$  100 m. Considering the number of outliers present, we defined the average deformation curve  $D_2(t)$  using a threshold of one standard deviation from the most extreme value.

Finally, the absolute displacement differences (ADD) can be calculated.

$$ADD_{1i}(t) = P1(t) - D_i(t) \quad i = 1, 2 \quad (7)$$

$$ADD_{2i}(t) = P2(t) - D_i(t) \quad i = 1, 2 \quad (8)$$

where  $P1(t)$  is the displacement of P1 in day  $t$ ,  $ADD_{1i}(t)$  is the deformation of PrP-P1 ( $i = 1$ ) or PrA-P1 ( $i = 2$ ).  $P2(t)$  is the displacement of P2 in day  $t$ ,  $ADD_{2i}(t)$  is the deformation of PrP-P2 ( $i = 1$ ) or PrA-P2 ( $i = 2$ ).

### 3.4. Remote Sensing Images

The Google Earth images were acquired by the SPOT satellite with a spatial resolution generally less than 5 m [59]. The Gaofen-2 image is a provided by Gansu Data and Application Center for High-resolution Earth Observation System [60]. Considering cloud-free, snow cover and obtainable high-resolution images, we selected Google Earth images in December 2010 and October 2013, and a Gaofen-2 in December 2016. These available images facilitated our visual identification of the study area and the landslide.

### 3.5. Local Precipitation and Soil Sampling

Our daily precipitation datasets were pulled from Version 3.0 of “Daily Surface Climate Variables of China” [61], which were used to analyze the inducing factors of landslide.

Meanwhile, we used 100 mL ring samplers to collect soil samples for the volume content and dry density measurements (Table S2). The sampling sites were located on the top, right, and bottom sides of landslide, and the pits had a maximum depth of 1.2 m. Soil data were used to describe soil moisture and texture during landslide occurrence.

## 4. Results

### 4.1. InSAR Landslides Analysis

The InSAR measurements (Figure 3a) showed that our study area mainly shows settlement in 2016–2017. Surface velocities ranged from  $-112$  to  $63$  mm/yr in the vertical direction (VD), with a mean of  $-11.8$  mm/yr and a standard deviation of  $12.0$  mm/yr. The subsidence signals accounted for 95.0% of the recorded movement. About 50% of the study area remained stable, with less than 1 cm/yr of

motion, while 1.1% of our study area experienced rapid surface velocities of more than 50 mm/yr. The white pixels represent a lack of data due to temporal decorrelation.

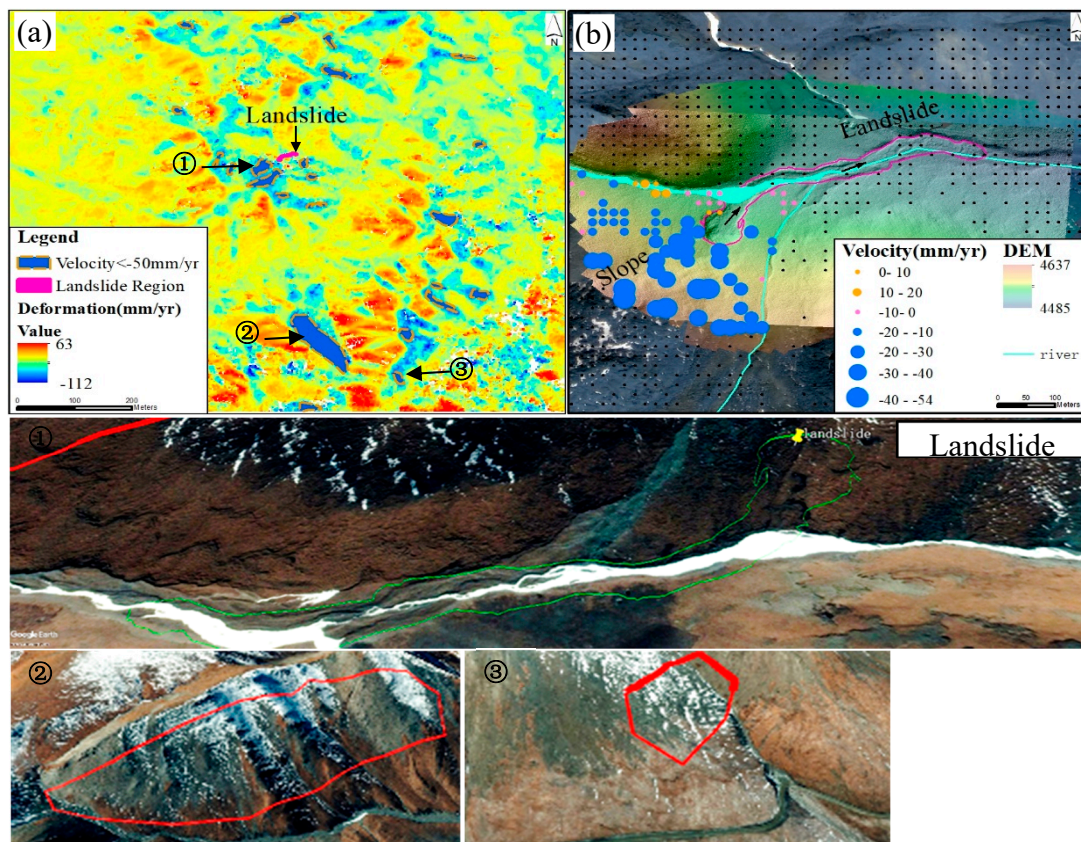


**Figure 3.** The vertical deformation velocity (VDV, mm/year) of the region based on the (a) pixels and the (b) point. The arrows indicate the direction of landslide flow in the DEM (30 cm  $\times$  30 cm) detected by the UAV. ①, ② and ③ are the fast creep ( $>50$  mm/yr) regions in Google Earth.

Creep is an important characteristic in the early stage of a landslide; we selected the unstable regions with fast creep ( $>50$  mm/yr) for further analysis (Figure 3a, red-dotted line). Based on the Google Earth images, we found that the subsidence mainly occurred in the middle of the mountain, and that uplift occurred at the gentle mountaintop. In Figure 3b, large creep (20–50 mm/yr) deformation occurred in the upper part of the landslide area along the slope direction, smaller amounts of creep (10–30 mm/yr) occurred on the sides, and positive stable deformation occurred in the middle and lower parts of the sliding body.

#### 4.2. Landslide Characteristics

From our analysis, we can see that the slope displacement is abnormal. In Figure 4a, we selected a section of the landscape along the slope, from the valley to the mountaintop for additional study. As the elevation decreased, the ground became increasingly unstable, and the landslide flow rate increased dramatically to 30 mm/yr at elevations of 4550–4570 m. The deformation and the slope change are strongly correlated above an elevation of 4550 m (Figure 4b); more than 50 mm/yr displacement occurred at 4530–4550 m, where the landslide initiated. It is possible that snowmelt water and high levels of precipitation and infiltration played a key role in the downward migration of the soil mass. Then the surface gradually stabilized in the valley.

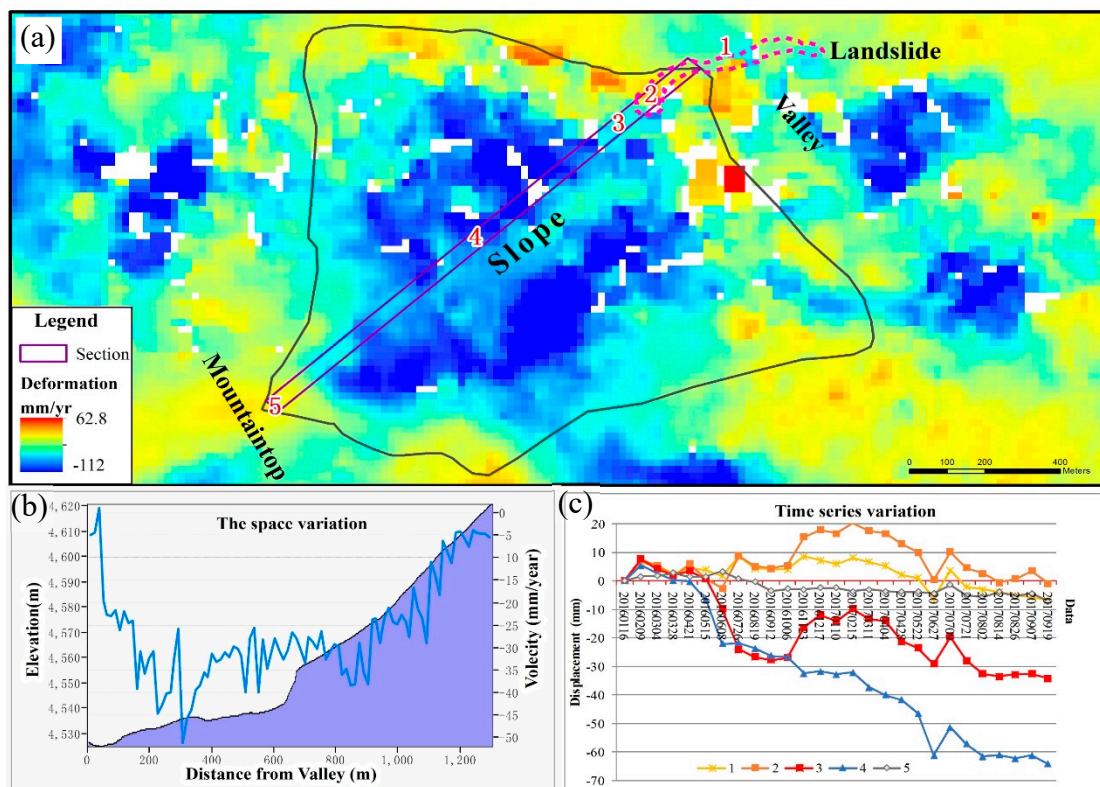


**Figure 4.** Deformation (a) acquired from InSAR in (b) space and (c) time. The purple rectangle represents the section area (about 1300 m long, 40 m wide) from the valley to the mountaintop; the red line represents the landslide. Point 2 and 3 were the same as P1 and P2 in Figure 1c, respectively.

In Figure 4c, five representative points were selected to show the cumulative displacements at different times. In the landslide area, curves 2 and 3 suddenly shifted in opposite directions between May and July 2016, and then followed similar trajectories afterwards. Curve 4 decreased steadily in a linear pattern. Curve 5, which tracked the bedrock, stayed relatively stable throughout the landslide, while the displacement of curve 1 increased and then decreased, due to soil accumulation and rock weathering, respectively.

#### 4.3. Quantification of Absolute Surface Displacements

Figure 5 showed the relative displacement time series of the freeze thaw cycles and local conditions in the landslide area. The PrP curve (blue line) represents the sinusoidal fits to the surface movement during an freeze thaw cycle for a frozen period ( $y = 11 \cdot \sin(\pi \cdot (x - 1)/5)$ ) and a thaw period ( $y = 10 \cdot \sin(\pi \cdot x/6)$ ) with high confidence in the correlation coefficient ( $R = 0.897$ ) and absolute error index (0.6 mm). The PrA curve represents the surface deformation process affected by LCs. This area, which contains 16 points, is about 100 m from the landslide, has the same elevation as the landslide, and a lateral extent of 100 m  $\times$  100 m. Using a threshold of one standard deviation (2.2 mm/year) from the most extreme value, we chose 12 points to define the average deformation curve (grey line).



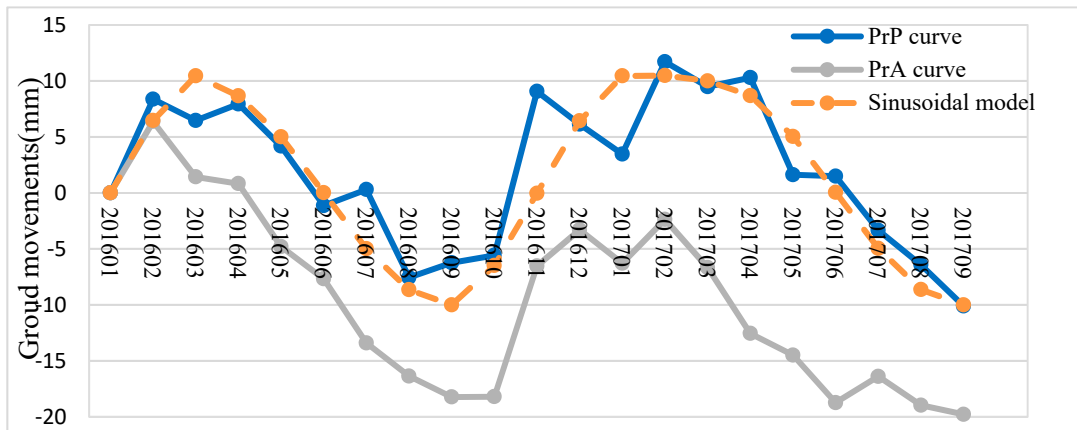


**Figure 5.** Displacement time series of the reference point (PrP, blue line) and the reference area (PrA, grey line) near the landslide (Figure 1c). The superimposed dotted curve (orange) and lines (red and green) represent predictions of the sinusoidal and linear models that best match the displacement values, respectively. Each point denotes a 20 m × 20 m pixel.

Based on these data, we mapped the surface absolute displacement differences (Figure 6). In Section 4.2, we discussed the opposing patterns at the top and the toe of the landslide; we selected two representative points (P1 and P2, Figure 1c) to study the evolution of the landslide since 2016. P1 and P2 also show an inverse pattern. After accounting for PrP, the PrP-P1 and PrP-P2 curves are relatively gentle, but beyond this, the trends and displacement lines follow similar trajectories. After removing PrA, the PrA-P1 and PrA-P2 curves became smooth lines with ~5 mm of ground movement until May of 2017. These data indicate that (1) other than three instances of noticeable creeps—May 2016, July 2016, and May 2017—the area maintained a relatively steady state and (2) PrA-P1 and PrA-P2 show that LCs other than the freeze-thaw cycle may be responsible for as much as 13 mm of displacement.

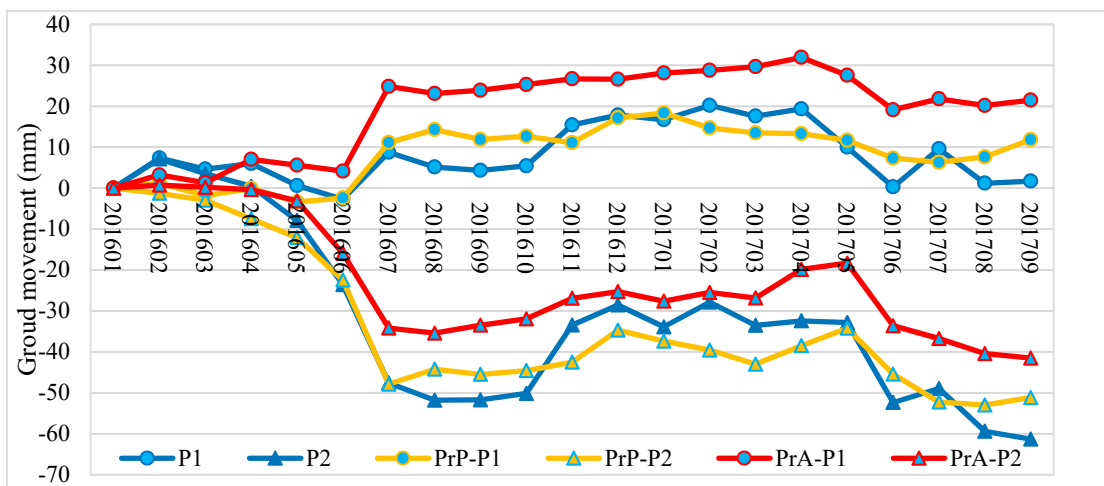


**Figure 6.** The absolute displacement differences between the landslide and the surrounding area with respect to the reference locations (PrP and PrA). The representative points P1 and P2 at different times for PrP or PrA are plotted as curves: PrP-P1 or PrA-P1 and PrP-P2 or PrA-P2, respectively.

#### 4.4. Interpreted Kinematics-based Failure Mechanism through the Satellite InSAR Data

Based on the SAR displacements and the stages of failure, a concept of kinematics-based failure mechanism for our small-scale landslide was mapped. We classified the landslide process into three

dynamic stages: primary creep, secondary creep, and tertiary creep, where creep represents the change in displacement over time.

The first stage consisted of primary creep along an unstable surface. The ground exhibited a motion state along the slope by gravity. In this study area, the unstable surface was defined by the fast creep areas (>50 mm/year); we discovered evidence of additional creep and older landslides near the fast creep areas along the road and the river (Figure 3a①,③). The fact that the toe has been excavated, collapsed, and scoured may contribute to the slope instability. These areas represent geohazards because these surfaces may also be critically unstable. Usually, rapid primary creep creates radial cracks or transient faulting (Figure 1d, Figure S1) in the unstable areas characterized by rapidly decreasing strain rates. Using our InSAR data (Figure 4b,c), we also observed noticeable deformation in the landslide area before the landslide occurred. With these types of these observations, it should be possible to implement early warning systems prior to slope failure.

The period of secondary creep was characterized by steady-state motion with a constant strain rate and limited equilibrium. The deformation of the surface was heterogeneous when the extrusion force or the friction coefficient becomes larger gradually. From May to July of 2016, the surface displacements showed that the top of the slope was sinking while the foot of the slope was rising (see Sections 4.3 and 4.4). As shown by the P1 and P2 SAR displacements, the ground was in a steady state (PrA-P1, PrA-P2), excluding the effect of local conditions and the freeze thaw cycle, to which we attribute 10–11 mm of ground motion. This stage was a progressive failure process with stress relaxation.

After a period of relative stability, the tertiary creep involved an increasing creep rate that eventually led to rupturing. Once triggering events e.g., the amount of water within the landslide, possibly due to rainfall conditions, reached the threshold, the landslide either accelerates until collapse occurs ① in Figure 7, or accelerates, and then reaches a new equilibrium ② in Figure 7.

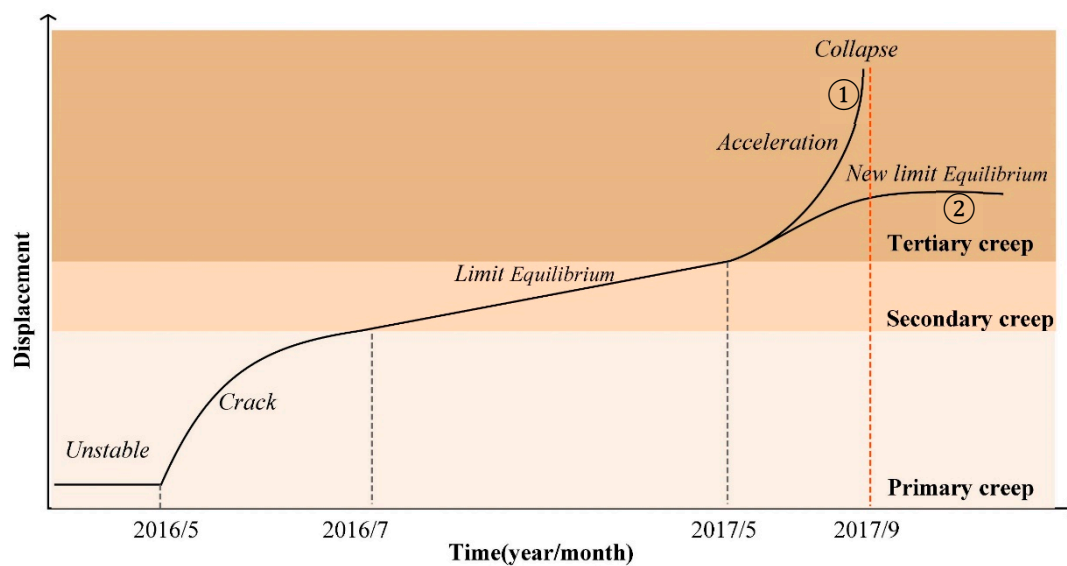


**Figure 7.** A concept map of Kinematics-based failure mechanisms for small-scale landslide.

## 5. Discussion

### 5.1. Landslide Causal Factors and Deformation Mechanism

The initiation of landslides is the result of multiple factors, including intrinsic factors that determine soil structure and slope stability (like topography, geology and soil regolith) and extrinsic factors that can change soil shear strength and lead to slope failure ultimately like rainfall [44,62]. The rainfall variables (intensity-duration, cumulated event rainfall and rainfall duration) were common to study the relationship between rainfall and landslide occurrences. In the study area, the cumulative rainfall exceeded 120 mm during 1 August 2017 and the time of the landslide event, about 33 mm more

than the same period in 2016 (Figure S2). This value was greater than the average rainfall (105 mm, 2012–2017) in the same period in the area. Before the landslide event, our study area also experienced prolonged rainfall for 5 days with a maximum daily rainfall about 19 mm and a mean cumulative rainfall of 38 mm (Figure S2). In this condition, it could alter the pore-water pressures and decrease soil strength [63]. Additionally, the u-shaped valley with large gradient (about 22°) (Figure 1) was favorable for the confluence of rainfall and snowmelt to flow into a landslide. The landslide material consisted of fine-grained soil and weathered rock, which promoted the permeation of water into the surface and the groundwater [64]. Meanwhile, the fractures (Figure S1) offered additional pathways for water to enter the soil. In short, the increased cumulative rainfall and persistent rainfall event exceeded the warning thresholds, then the soil with the high-water content over 0.46 (Table S2) was lost all shear strength and suddenly liquefied, destroying large areas and flowing for several kilometers.

Slow-moving landslides responded typically to precipitation by increasing pore-water pressure that leads to the long term uplift [63,65]. The total deformation and the rainfall over 24 days can be found a remarkable consistency between June and October in Figure 8. Many other studies also reached the same conclusion [66,67], but there was something different that it was large displacement in time of poor rainfall. Maybe it was affected by strong freeze thaw cycle in frozen ground regions, which proved by the relationship between the deformation and temperature.

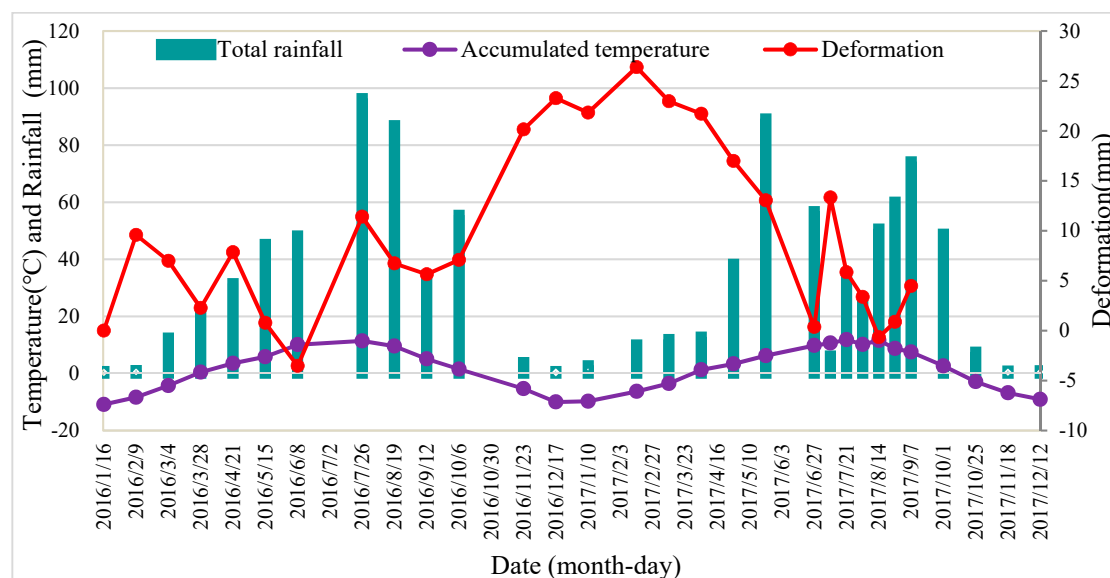


**Figure 8.** The total temperature, rainfall and deformation of landslide (P1, Figure 1c) over 24 days. The total temperature and rainfall are the average data of the Yushu and Qingshuihe meteorological stations during the same periods.

## 5.2. Quantifying Landslide Activity and InSAR Signal Separation

InSAR showed the operational potential to detect small-scale landslides in some dynamic process of landslide in time and space. In Figures 3 and 4, it was evident that representative moving points in landslides had more than one break in time series, which may relate to temperature, snowmelt and rainfall. Our study area was in the Qinghai-Tibetan Plateau with intense and frequent freeze–thaw actions leading to the creep or frost shifting. During April to May, the thaw subsidence and freezing uplift changed one cycle every day [68], maybe making the entire slope unstable [69,70]. Numerous studies in Arctic and mountain area suggested that freeze thaw cycle and snow melt induced landslide occurrence in the following spring–summer [71–74]. After June, the rapid increase of precipitation and thaw depth led to the occurrence of landslides, becoming the main controlling factor of deformation (Figure 8). The events were widespread in subarctic and Arctic areas [75,76], Siberia [77] and

Qinghai-Tibet [78] and attributable to anomalously high air temperature and high precipitation during the thawing season in these years.

SAR interference techniques, which depended on a phase change to demonstrate relative deformation information, were widely used to monitor landslide. However, the slope stability depended on the intrinsic factors and the slope unstable depended on the extrinsic factors, like weathering, tectonic events, or human impact on the slope. While the slope finally failed determination by triggering factors such as rainfall, snowmelt or earthquakes [44,62]. Therefore, the relative deformation cannot veritably reflect the movement process in different environments. We proposed a new method to quantify absolute deformation to describe the actual movement process of landslide. This method relied on actual physical processes and laws, e.g., freeze thaw cycle and others. Different factors were separated from SAR signals to reveal their influence on landslide. Based on the new model, when freeze thaw cycle and local conditions were separated, more details of landslide changes were successfully detected, such as three instances of noticeable creeps—May 2016, July 2016, and May 2017. However, compared with the permafrost regions summarized by Zhang [79], the seasonal amplitude of freeze thaw cycle in our study area was relatively small. Therefore, further measurements or observations were required to verify the results. The spatial variability in Figure 6 and Table S1 also suggest that the dynamics of the landslide were not controlled by any single factor, but by a combination of many factors, possibly including the soil structure and/or the soil moisture concentration. While InSAR cannot provide any soil depth information, which had to be supplemented by geophysical data or numerical models [80]. In fact, a combination of landslide susceptibility maps was advisable [81].

Three instances of noticeable creeps (e.g., May 2016, July 2016, and May 2017 in Figures 4c and 6) maybe related to particular meteorological trends, but it was obviously the actual movements of landslide in Figure 6. Because when we quantified the absolute deformation, the relative atmospheric effects can also be removed, but the creeps were remaining. While the deformation trend in June 2017 maybe the atmospheric effects, which was removed.

### 5.3. InSAR Technique Using in Frozen Ground

Based on InSAR monitoring data, we applied a sinusoidal model to fit the freeze thaw seasonal displacements and then quantified the absolute deformation of the landslide area. Some landslide details had been successfully detected by separated the signals. We can call it the process of the absolute deformation signal separation. This method framework for studying the landslide process was easy to follow and with strong application, give more practical guidance for research on permafrost or seasonally frozen ground.

In frozen ground regions, the surface displacements were the result of multiple factors. As Strozzi [82] stated in research of low-land permafrost: we had to bear in mind that the maps and graphs measured by SAR not only represent surface displacement but also changes in ionospheric, soil moisture, snow-cover and vegetation conditions. Some researches, as shown in Table 2, tried to separate the factors to explain the relationship between the factors and deformation to further reveal the mechanism and process in permafrost region. Some laws and processes can be summarized in Figure 9 to improve the general applicability of our method. Thus, we tried to improve the deformation model (Equation (5)) in frozen ground regions as:

$$D(t) = D_{season}(t) + K(t) + C \quad (9)$$

**Table 2.** Parameters of previous studies in global frozen ground region using SAR satellite.

Location	Dataset	Environment Condition	Reference & Validation	Time Period	Amplitude of Deformation	Factors Discussion	Authors
Arctic and Antarctic	Sentinel-1	Low-land permafrost	In-situ, TerraSAR-X	201711-201812	3–10 cm	Deformation validation	Strozzi et al. 2018 [82]
Eastern Canada	RadarSat-2	Continuous permafrost	Bedrock	201105-201109	0–6.5 cm	Soil moisture	Short et al. 2013 [84]
Southwestern Alaska	ALOS	Discontinuous permafrost	Absolute phase calculated by ALT	200712-201002	0–4 cm	Wildfire	Michaelides et al. 2019 [83]
Northwestern Qinghai Tibet	Envisat	Discontinuous permafrost	Bedrock	2003–2011	0–1.2 cm	Soil moisture	Daout et al. 2017 [48]
Central Qinghai-Tibet Plateau	Sentinel-1	Permafrost region	ALT	201711-201812	0.2–3 cm	Active layer, land covers	Zhang et al. 2019 [79]
Eastern Qinghai-Tibet Plateau	Sentinel-1	Permafrost, seasonally frozen ground	Bedrock, high-coherence	201601-201709	0–11 cm	Freeze thaw cycle, rainfall	this study area
Qinghai-Tibet highway(G214)	TerraSAR-X	Permafrost, seasonally frozen ground	Unkown	201508-201508	0–10 cm	Freeze thaw cycle	Dai et al. 2018 [85]

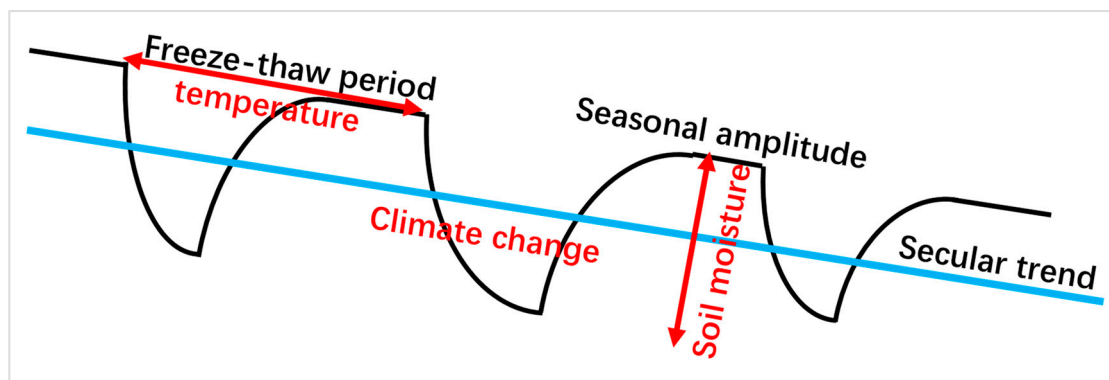


**Figure 9.** Deformation decomposed into seasonal (e.g., freeze thaw period) and secular trend (e.g., climate change) in permafrost regions. Modified from Michaelides et al. 2019 [83]. The period was controlled by the temperature, while the amplitude was determined by the soil moisture.

In order to understand this formula, we mapped a conceptual diagram (Figure 9) of the deformation process in frozen ground regions. The surface displacement  $D(t)$  decomposed into seasonal and secular trend.  $D_{season}(t)$  are the deformation during the freeze thaw period, which can be described by sinusoidal function [48,79], Stefan [83] or others. The period is the accumulated degree days of thawing/freezing related to the temperature. While  $A$  and  $B$  are deformation associated with the seasonal thawing/freezing of the active layer (ALT), mainly affected by the soil moisture [48,84,85].  $K(t)$  was the secular trend, showing a linear [48,83] or non-linear relationship [83]. This trend is related to climate warming [48], landcover [79], ice losing, wildfire [83], etc.

In the process of measurement, error description was essential. Only a thorough validation with in-situ data would permit full quantitative assessment of the displacement maps [82]. Bedrock was a commonly used reference, followed by LiDAR, GPS point, artificial reflectors and intercompare results from different sensors. However, no spatial correspondence often be observed between InSAR and the reference measurements due to soil moisture [86] and others, time consistency between measurement and satellite transit and ground resolution. While quantification of absolute surface displacements was a good method for data rationality verification [79,83].

## 6. Conclusions

InSAR (SBAS) method and the absolute deformation model are suitable for monitoring the small-scale landslides in the frozen ground area. We proposed the methodical steps for the calculation of absolute displacement of the landslide and employed the implementation of data into a diagram explaining “Kinematics-based failure mechanisms for small-scale landslide are in the creeping and sliding stages, which eventually lead to the failure stage”. Finally, we highlight an advanced absolute deformation model suitable for frozen ground regions to describe the seasonal and secular trend in frozen ground regions. This method framework of the InSAR signal separation is easy to follow and with strong application, give more practical guidance for research on permafrost or seasonally frozen ground. Although the absolute deformation model has been used to explain some factors, e.g. Freeze-thaw cycle, it must be supplemented by depth information from geophysical data or numerical models in site to further verification.

Previous work has shown that multi-source remote sensing methods can detect fast-moving landslide [18,19], capture clear morphological evidence [87] and insight the kinematics and their potential controls from hourly to decadal timescales [31]. All of these techniques have their advantages and can be combined with Geography information system (GIS) technology to determine the susceptibility of an area to landslide hazards. Further efforts should be made to model landslides using a combination of physical models, detailed field measurements, and remote techniques.

**Supplementary Materials:** The following are available online at <http://www.mdpi.com/2072-4292/11/18/2126/s1>, Figure S1: Images of landslide area. Images of the landslide area are shown from (a) December 2010 (Google Earth), (b) October 2013 (Google Earth), (c) December 2016 (GF-2), and (d) September 2017 (UAV). Red curves represent the boundary of landslide. Table S1: Soil properties based on field investigation in the slide area on Sept. 10, 2017.

**Author Contributions:** Conceptualization and methodology, T.H.W., L.Z., X.D.W. and J.M.H.; Formal Analysis, G.J.H., R.L. and C.W.X.; Software, J.M.H. and J.N.; Investigation, X.D.W., X.F.Z. and J.M.H.; Writing-Original Draft Preparation, J.M.H. and T.H.W.; Writing-Review & Editing T.H.W., D.F.Z. and J.M.H.; Visualization, C.Y., X.F.L. and W.S.M.; Funding Acquisition, T.H.W.

**Funding:** This study was funded by the Strategic Priority Research Program of Chinese Academy of Sciences (Grant No. XDA20030201; XDA23060703), the National Natural Science Foundations of China (41690142; 41771076; 41671070; 41701073).

**Acknowledgments:** The supports from the Cryosphere Research Station on the Qinghai-Tibetan Plateau are especially appreciated. The data are provided by the European Space Agency (ESA, <https://scihub.copernicus.eu>), the United States Geological Survey (USGS, <https://earthexplorer.usgs.gov>), the China Meteorological Administration (CMA, <http://data.cma.cn/>).

**Conflicts of Interest:** The authors declare no conflict of interest.

## References

1. Yao, T.; Xue, Y.; Chen, D.; Chen, F.; Thompson, L.; Cui, P.; Koike, T.; Lau, W.K.M.; Lettenmaier, D.; Mosbrugger, V.; et al. Recent third pole's rapid warming accompanies cryospheric melt and water cycle intensification and interactions between monsoon and environment: Multidisciplinary approach with observations, modeling, and analysis. *Bull. Am. Meteorol. Soc.* **2018**, *100*, 423–444. [[CrossRef](#)]
2. Chen, D.; Xu, B.; Yao, T.; Guo, Z.; Cui, P.; Chen, F.; Zhang, R.; Zhang, X.; Zhang, Y.; Fan, J.; et al. Assessment of past, present and future environmental changes on the Tibetan Plateau. *Chin. Sci. Bull.* **2015**, *60*, 3025–3035.
3. Cui, P.; Jia, Y. Mountain hazards in the Tibetan Plateau: Research status and prospects. *Natl. Sci. Rev.* **2015**, *2*, 397–399. [[CrossRef](#)]
4. Ding, Y.; Zhang, S.; Zhao, L.; Li, Z.; Kang, S. Global warming weakening the inherent stability of glaciers and permafrost. *Sci. Bull.* **2019**, *64*, 245–253. [[CrossRef](#)]
5. Sun, Z.; Wang, Y.; Sun, Y.; Niu, F.; Li, G.; Gao, Z. Creep characteristics and process analyses of a thaw slump in the permafrost region of the Qinghai-Tibet Plateau, China. *Geomorphology* **2017**, *293*, 1–10. [[CrossRef](#)]
6. Ward Jones, M.K.; Pollard, W.H.; Jones, B.M. Rapid initialization of retrogressive thaw slumps in the Canadian high Arctic and their response to climate and terrain factors. *Environ. Res. Lett.* **2019**, *14*, 055006. [[CrossRef](#)]

7. Gao, Z.; Niu, F.; Wang, Y.; Luo, J.; Lin, Z. Impact of a thermokarst lake on the soil hydrological properties in permafrost regions of the Qinghai-Tibet Plateau, China. *Sci. Total Environ.* **2017**, *574*, 751–759. [[CrossRef](#)]
8. Yang, M.; Wang, X.; Pang, G.; Wan, G.; Liu, Z. The Tibetan Plateau cryosphere: Observations and model simulations for current status and recent changes. *Earth Sci. Rev.* **2019**, *190*, 353–369. [[CrossRef](#)]
9. Cheng, G.; Wu, T. Responses of permafrost to climate change and their environmental significance, Qinghai-Tibet Plateau. *J. Geophys. Res. Earth Surf.* **2007**, *112*, 1–10. [[CrossRef](#)]
10. Zhao, L.; Marchenko, S.S.; Sharkhuu, N.; Wu, T. Regional changes of permafrost in Central Asia Qinghai-Tibet Plateau in China. *Proc. Ninth Int. Conf. Permafrost.* **2008**, *29*, 2061–2069.
11. The International Disaster Database. Available online: <https://www.emdat.be/database> (accessed on 10 April 2019).
12. Lin, Q.; Wang, Y. Spatial and temporal analysis of a fatal landslide inventory in China from 1950 to 2016. *Landslides* **2018**, *15*, 2357–2372. [[CrossRef](#)]
13. Mikosš, M.; Casagli, N.; Yin, Y.; Sassa, K. *Advancing Culture of Living with Landslides: Volume 1 ISDR-ICL Sendai Partnerships 2015–2025*; Springer: Berlin/Heidelberg, Germany, 2017; Volume 5, ISBN 3319534858.
14. Bowman, E.T. *Small Landslides-Frequent, Costly, and Manageable*; Elsevier Inc: Amsterdam, The Netherlands, 2014; ISBN 9780123964755.
15. Luo, J.; Yin, G.; Niu, F.; Lin, Z.; Liu, M. High spatial resolution modeling of climate change impacts on permafrost thermal conditions for the Beiluhe Basin, Qinghai-Tibet Plateau. *Remote Sens.* **2019**, *11*, 1294. [[CrossRef](#)]
16. Wu, Q.; Shi, B.; Fang, H.Y. Engineering geological characteristics and processes of permafrost along the Qinghai-Xizang (Tibet) Highway. *Eng. Geol.* **2003**, *68*, 387–396. [[CrossRef](#)]
17. Leandro, G.; Mucciarelli, M.; Pellicani, R.; Spilotro, G. Monitoring of large instable areas: System reliability and new tools. *EGU Gen. Assem. Conf. Abstr.* **2009**, *11*, 10961.
18. Metternicht, G.; Hurni, L.; Gogu, R. Remote sensing of landslides: An analysis of the potential contribution to geo-spatial systems for hazard assessment in mountainous environments. *Remote Sens. Environ.* **2005**, *98*, 284–303. [[CrossRef](#)]
19. Zhao, C.; Lu, Z. Remote sensing of landslides—A review. *Remote Sens.* **2018**, *10*, 8–13. [[CrossRef](#)]
20. Mora, O.; Liu, J.; Lenzano, M.; Toth, C.; Grejner-Brzezinska, D. Small landslide susceptibility and hazard assessment based on airborne lidar data. *Photogramm. Eng. Remote Sens.* **2015**, *81*, 239–247. [[CrossRef](#)]
21. Holec, J.; Bednarik, M.; Šabo, M.; Minár, J.; Yilmaz, I.; Marschalko, M. A small-scale landslide susceptibility assessment for the territory of Western Carpathians. *Nat. Hazards* **2013**, *69*, 1081–1107. [[CrossRef](#)]
22. Fernández, T.; Pérez, J.; Colomo, C.; Cardenal, J.; Delgado, J.; Palenzuela, J.; Irigaray, C.; Chacón, J. Assessment of the evolution of a landslide using digital photogrammetry and LiDAR techniques in the Alpujarras Region (Granada, Southeastern Spain). *Geosciences* **2017**, *7*, 32. [[CrossRef](#)]
23. Caris, J.P.T.; Van Asch, T.W.J. Geophysical, geotechnical and hydrological investigations of a small landslide in the French Alps. *Eng. Geol.* **1991**, *31*, 249–276. [[CrossRef](#)]
24. Bovenga, F.; Pasquariello, G.; Pellicani, R.; Refice, A.; Spilotro, G. Landslide monitoring for risk mitigation by using corner reflector and satellite SAR interferometry: The large landslide of Carlantino (Italy). *Catena* **2017**, *151*, 49–62. [[CrossRef](#)]
25. Carlà, T.; Tofani, V.; Lombardi, L.; Raspini, F.; Bianchini, S.; Bertolo, D.; Thuegaz, P.; Casagli, N. Combination of GNSS, satellite InSAR, and GBInSAR remote sensing monitoring to improve the understanding of a large landslide in high alpine environment. *Geomorphology* **2019**, *335*, 62–75. [[CrossRef](#)]
26. Calò, F.; Calcaterra, D.; Iodice, A.; Parise, M.; Ramondini, M. Assessing the activity of a large landslide in southern Italy by ground-monitoring and SAR interferometric techniques. *Int. J. Remote Sens.* **2012**, *33*, 3512–3530. [[CrossRef](#)]
27. Qi, S.; Zou, Y.; Wu, F.; Yan, C.; Fan, J.; Zang, M.; Zhang, S.; Wang, R. A recognition and geological model of a deep-seated ancient landslide at a reservoir under construction. *Remote Sens.* **2017**, *9*, 383. [[CrossRef](#)]
28. Strozzi, T.; Klimeš, J.; Frey, H.; Caduff, R.; Huggel, C.; Wegmüller, U.; Rapre, A.C. Satellite SAR interferometry for the improved assessment of the state of activity of landslides: A case study from the Cordilleras of Peru. *Remote Sens. Environ.* **2018**, *217*, 111–125. [[CrossRef](#)]
29. Barboux, C.; Strozzi, T.; Delaloye, R.; Wegmüller, U.; Collet, C. Mapping slope movements in Alpine environments using TerraSAR-X interferometric methods. *ISPRS J. Photogramm. Remote Sens.* **2015**, *109*, 178–192. [[CrossRef](#)]

30. Corsini, A.; Farina, P.; Antonello, G.; Barbieri, M.; Casagli, N.; Coren, F.; Guerri, L.; Ronchetti, F.; Sterzai, P.; Tarchi, D. Space-borne and ground-based SAR interferometry as tools for landslide hazard management in civil protection. *Int. J. Remote Sens.* **2006**, *27*, 2351–2369. [[CrossRef](#)]
31. Berti, M.; Corsini, A.; Franceschini, S.; Iannaccone, J.P. Automated classification of persistent scatterers interferometry time series. *Nat. Hazards Earth Syst. Sci.* **2013**, *13*, 1945–1958. [[CrossRef](#)]
32. Colesanti, C.; Wasowski, J. Investigating landslides with space-borne synthetic aperture radar (SAR) interferometry. *Eng. Geol.* **2006**, *88*, 173–199. [[CrossRef](#)]
33. Ferretti, A.; Prati, C.; Rocca, F.; Politecnico, I. Permanent scatterers in SAR interferometry. *IEEE Trans. Geosci. Remote Sens.* **1999**, *39*, 1528–1530.
34. Berardino, P.; Fornaro, G.; Lanari, R.; Sansosti, E. A new algorithm for surface deformation monitoring based on small baseline differential SAR interferograms. *IEEE Trans. Geosci. Remote Sens.* **2002**, *40*, 2375–2383. [[CrossRef](#)]
35. Barboux, C.; Delaloye, R.; Lambiel, C. Inventorying slope movements in an Alpine environment using DInSAR. *Earth Surf. Process. Landforms* **2014**, *39*, 2087–2099. [[CrossRef](#)]
36. Zhou, X.; Chang, N.B.; Li, S. Applications of SAR interferometry in earth and environmental science research. *Sensors* **2009**, *9*, 1876–1912. [[CrossRef](#)]
37. The Copernicus Open Access Hub. Available online: <https://scihub.copernicus.eu/dhus/#/home> (accessed on 3 September 2018).
38. Yin, Y.; Ma, Y.; Ma, Y.; Hu, D.; Zhang, Z. Rapid Identification and Emergency Investigation of Surface Ruptures and Geohazards Induced by the Ms 7.1 Yushu Earthquake. *J. Eng. Geol.* **2010**, *84*, 289–296.
39. Zhang, X. Snow Monitoring and Early Warning of Snow Disaster in Pastoral Areas of Qinghai Province. Ph.D. Thesis, Lanzhou University, Lanzhou, China, 2016.
40. Zou, D.; Zhao, L.; Sheng, Y.; Chen, J.; Hu, G.; Wu, T.; Wu, J.; Xie, C.; Wu, X.; Pang, Q.; et al. A new map of permafrost distribution on the Tibetan Plateau. *Cryosphere* **2017**, *11*, 2527–2542. [[CrossRef](#)]
41. Gao, B.; Wang, J.; Zhang, C.; Feng, W. Formation mechanism of rainstorm-induced debris flow in Yushu state of Qinghai Province—a case study on debris flow of Lalong Gully in Chengduo county. *Bull. Soil Water Conserv.* **2016**, *36*, 28–31.
42. Zhimei Landslide. Available online: <http://www.yushunews.com/system/2017/09/09/012410991.shtml> (accessed on 9 September 2017).
43. Zhimei Landslide (Video). Available online: <http://www.jiaomomo.com/forum.php?mod=viewthread&tid=353932> (accessed on 9 September 2017).
44. Highland, L.M.; Bobrowski, P. *The Landslide Handbook—A Guide to Understanding Landslides*; US Geological Survey Circular: Reston, VA, USA, 2008; Volume 1325, p. 129.
45. The United States Geological Survey, USGS. Available online: <http://earthexplorer.usgs.gov/> (accessed on 3 September 2018).
46. PHANTOM 4 PRO. Available online: <https://www.dji.com/cn/phantom-4-pro> (accessed on 3 September 2018).
47. Doin, M.P.; Lasserre, C.; Peltzer, G.; Cavalié, O.; Doubre, C. Corrections of stratified tropospheric delays in SAR interferometry: Validation with global atmospheric models. *J. Appl. Geophys.* **2009**, *69*, 35–50. [[CrossRef](#)]
48. Daout, S.; Doin, M.; Peltzer, G.; Socquet, A.; Lasserre, C. Large scale InSAR monitoring of permafrost freeze-thaw cycles on the Tibetan Plateau. *Geophys. Res. Lett.* **2017**, *44*, 1–16. [[CrossRef](#)]
49. Sentinel-1 Quality Control. Available online: <https://qc.sentinel1.eo.esa.int/> (accessed on 3 September 2018).
50. Zhang, L.; Ding, X.; Lu, Z.; Jung, H.S.; Hu, J.; Feng, G. A novel multitemporal insar model for joint estimation of deformation rates and orbital errors. *IEEE Trans. Geosci. Remote Sens.* **2014**, *52*, 3529–3540. [[CrossRef](#)]
51. Ducret, G.; Doin, M.P.; Grandin, R.; Lasserre, C.; Guillaso, S. DEM corrections before unwrapping in a small baseline strategy for InSAR time series analysis. *IEEE Geosci. Remote Sens. Lett.* **2013**, *11*, 696–700. [[CrossRef](#)]
52. Ferretti, A. *Satellite InSAR Data—Reservoir Monitoring from Space*; EAGE: Houten, The Netherlands, 2014; Volume 3, ISBN 9789073834712.
53. Wang, L.; Marzahn, P.; Bernier, M.; Jacome, A.; Poulin, J.; Ludwig, R. Comparison of TerraSAR-X and ALOS PALSAR differential interferometry with multisource DEMs for monitoring ground displacement in a discontinuous permafrost region. *IEEE J. Sel. Top. Appl. Earth Obs. Remote Sens.* **2017**, *10*, 4074–4093. [[CrossRef](#)]



54. Pepe, A.; Lanari, R. On the extension of the minimum cost flow algorithm for phase unwrapping of multitemporal differential SAR interferograms. *IEEE Trans. Geosci. Remote Sens.* **2006**, *44*, 2374–2383. [[CrossRef](#)]
55. Zuo, J.; Gong, H.; Chen, B.; Liu, K.; Zhou, C.; Ke, Y. Time-series evolution patterns of land subsidence in the Eastern Beijing Plain, China. *Remote Sens.* **2019**, *11*, 539. [[CrossRef](#)]
56. Wang, C.; Zhang, Z.; Zhang, H.; Zhang, B.; Tang, Y.; Wu, Q. Active layer thickness retrieval of Qinghai-Tibet permafrost using the TerraSAR-X InSAR Technique. *IEEE J. Sel. Top. Appl. Earth Obs. Remote Sens.* **2018**, *11*, 4403–4413. [[CrossRef](#)]
57. Liu, L.; Schaefer, K.; Zhang, T.; Wahr, J. Estimating 1992–2000 average active layer thickness on the Alaskan North Slope from remotely sensed surface subsidence. *J. Geophys. Res. Earth Surf.* **2012**, *117*, 1–14. [[CrossRef](#)]
58. Hu, G.; Zhao, L.; Wu, X.; Li, R.; Wu, T.; Xie, C.; Qiao, Y.; Shi, J.; Li, W.; Cheng, G. New Fourier-series-based analytical solution to the conduction-convection equation to calculate soil temperature, determine soil thermal properties, or estimate water flux. *Int. J. Heat Mass Transf.* **2016**, *95*, 815–823. [[CrossRef](#)]
59. Visser, V.; Langdon, B.; Pauchard, A.; Richardson, D.M. Unlocking the potential of google earth as a tool in invasion science. *Biol. Invasions* **2014**, *16*, 513–534. [[CrossRef](#)]
60. Gansu Data and Application Center for High-resolution Earth Observation System. Available online: <http://www.westgfdc.ac.cn/sysMng/> (accessed on 12 September 2017).
61. The China Meteorological Administration. Available online: <http://data.cma.cn> (accessed on 3 September 2018).
62. Zou, Q.; Cui, P.; He, J.; Lei, Y.; Li, S. Regional risk assessment of debris flows in China—An HRU-based approach. *Geomorphology* **2019**, *340*, 84–102. [[CrossRef](#)]
63. Bogaard, T.A.; Greco, R. Landslide hydrology: From hydrology to pore pressure. *Wiley Interdiscip. Rev. Water* **2016**, *3*, 439–459. [[CrossRef](#)]
64. Yalcin, A. GIS-based landslide susceptibility mapping using analytical hierarchy process and bivariate statistics in Ardesen (Turkey): Comparisons of results and confirmations. *CATENA* **2008**, *72*, 1–12. [[CrossRef](#)]
65. Schmidt, D.A.; Bürgmann, R. Time-dependent land uplift and subsidence in the Santa Clara valley, California, from a large interferometric synthetic aperture radar data set. *J. Geophys. Res. Solid Earth* **2003**, *108*, 1–13. [[CrossRef](#)]
66. Sun, Q.; Zhang, L.; Ding, X.L.; Hu, J.; Li, Z.W.; Zhu, J.J. Slope deformation prior to Zhouqu, China landslide from InSAR time series analysis. *Remote Sens. Environ.* **2015**, *156*, 45–57. [[CrossRef](#)]
67. Carlà, T.; Farina, P.; Intrieri, E.; Ketizmen, H.; Casagli, N. Integration of ground-based radar and satellite InSAR data for the analysis of an unexpected slope failure in an open-pit mine. *Eng. Geol.* **2018**, *235*, 39–52. [[CrossRef](#)]
68. Zhao, L.; Cheng, G.; Shuxun, L.I.; Zhao, X.; Wang, S. Thawing and freezing processes of active layer in Wudaoliang region of Tibetan Plateau. *Sci. Bull.* **2000**, *45*, 2181–2187. [[CrossRef](#)]
69. Darrow, M.M.; Daanen, R.P.; Gong, W. Predicting movement using internal deformation dynamics of a landslide in permafrost. *Cold Reg. Sci. Technol.* **2017**, *143*, 93–104. [[CrossRef](#)]
70. Xu, J.; Wang, Z.Q.; Ren, J.W.; Wang, S.H.; Jin, L. Mechanism of slope failure in loess terrains during spring thawing. *J. Mt. Sci.* **2018**, *15*, 845–858. [[CrossRef](#)]
71. Lopez, S.J.; Corona, C.; Stoffel, M.; Berger, F. Climate change increases frequency of shallow spring landslides in the French Alps. *Geology* **2013**, *41*, 619–622.
72. Bíl, M.; Müller, I. The origin of shallow landslides in Moravia (Czech Republic) in the spring of 2006. *Geomorphology* **2008**, *99*, 246–253. [[CrossRef](#)]
73. Moreiras, S.; Lisboa, M.S.; Mastrantonio, L. The role of snow melting upon landslides in the central Argentinean Andes. *Earth Surf. Process. Landforms* **2012**, *37*, 1106–1119. [[CrossRef](#)]
74. Balsler, A.W.; Gens, R.; Member, A.C.; Mack, M.C.; Member, A.C.; Walker, D.A.; Member, A.C.; Wagner, D.; Layer, P.W.; Eichelberger, J.C. Retrogressive Thaw Slumps and Active Layer Detachment Slides in the Brooks Range and Foothills of Northern Alaska Terrain and Timing. Ph.D. Thesis, University of Alaska Fairbanks, Fairbanks, AK, USA, 2015.
75. Lewkowicz, A.G.; Way, R.G. Extremes of summer climate trigger thousands of thermokarst landslides in a high arctic environment. *Nat. Commun.* **2019**, *10*, 1–11. [[CrossRef](#)]
76. Swanson, D.K.; Nolan, M. Growth of retrogressive thaw slumps in the Noatak Valley, Alaska, 2010–2016, measured by airborne photogrammetry. *Remote Sens.* **2018**, *10*, 2010–2016. [[CrossRef](#)]

77. Zwieback, S.; Kokelj, S.; Günther, F.; Boike, J.; Grosse, G.; Hajnsek, I. Sub-seasonal thaw slump mass wasting is not consistently energy limited at the landscape scale. *Cryosphere* **2018**, *12*, 549–564. [[CrossRef](#)]
78. Luo, J.; Niu, F.; Lin, Z.; Liu, M.; Yin, G. Recent acceleration of thaw slumping in permafrost terrain of Qinghai-Tibet Plateau: An example from the Beiluhe Region. *Geomorphology* **2019**, *341*, 79–85. [[CrossRef](#)]
79. Zhang, X.; Zhang, H.; Wang, C.; Tang, Y.; Zhang, B.; Wu, F.; Wang, J.; Zhang, Z. Time-series InSAR monitoring of permafrost freeze-thaw seasonal displacement over Qinghai-Tibetan Plateau using sentinel-1 data. *Remote Sens.* **2019**, *11*, 1000. [[CrossRef](#)]
80. Whiteley, J.S.; Chambers, J.E.; Uhlemann, S.; Wilkinson, P.B.; Kendall, J.M. Geophysical monitoring of moisture-induced landslides: A review. *Rev. Geophys.* **2019**, *57*, 106–145. [[CrossRef](#)]
81. Barra, A.; Monserrat, O.; Mazzanti, P.; Esposito, C.; Crosetto, M.; Scarascia Mugnozza, G. First insights on the potential of Sentinel-1 for landslides detection. *Geomatics Nat. Hazards Risk* **2016**, *7*, 1874–1883. [[CrossRef](#)]
82. Strozzi, T.; Antonova, S.; Günther, F.; Mätzler, E.; Vieira, G.; Wegmüller, U.; Westermann, S.; Bartsch, A. Sentinel-1 SAR interferometry for surface deformation monitoring in low-land permafrost areas. *Remote Sens.* **2018**, *10*, 1360. [[CrossRef](#)]
83. Michaelides, R.J.; Schaefer, K.; Zebker, H.A.; Parsekian, A.; Liu, L.; Chen, J.; Natali, S.; Ludwig, S.; Schaefer, S.R. Inference of the impact of wildfire on permafrost and active layer thickness in a discontinuous permafrost region using the remotely sensed active layer thickness (ReSALT) algorithm. *Environ. Res. Lett.* **2019**, *14*, 035007. [[CrossRef](#)]
84. Short, N.; Leblanc, A.M.; Sladen, W.; Brisco, B. RADARSAT-2 InSAR for monitoring permafrost environments: Pangnirtung and iqaluit. In Proceedings of the 2013 IEEE Radar Conference (RadarCon13), Ottawa, ON, Canada, 29 April–23 May 2013; pp. 4–7.
85. Dai, K.; Liu, G.; Li, Z.; Ma, D.; Wang, X.; Zhang, B.; Tang, J.; Li, G. Monitoring highway stability in permafrost regions with X-band temporary scatterers stacking InSAR. *Sensors* **2018**, *18*, 1876. [[CrossRef](#)]
86. Nolan, M.; Fatland, D.R. Penetration depth as a DInSAR observable and proxy for soil moisture. *IEEE Trans. Geosci. Remote Sens.* **2003**, *41*, 532–537. [[CrossRef](#)]
87. Le Bivic, R.; Allemand, P.; Quiquerez, A.; Delacourt, C. Potential and limitation of SPOT-5 ortho-image correlation to investigate the cinematics of landslides: The example of Mare à Poule d’Ea” (Réunion, France). *Remote Sens.* **2017**, *9*, 106. [[CrossRef](#)]

